

Ultrafast laser induced surface modification in absence of non-thermal melting and evaporation

G. D. Tsibidis^{1*}, M. Barberoglou¹, P. A. Loukakos¹, E. Stratakis¹, C. Fotakis^{1,2}

¹*Institute of Electronic Structure and Laser (IESL), Foundation for Research and Technology (FORTH), N. Plastira 100, Vassilika Vouton, 70013, Heraklion, Crete, Greece*

²*Physics Department, University of Crete, Heraklion 71409, Crete, Greece*

The present paper elucidates the physical mechanism that accounts for the principal/primary stages of the structuring process taking place upon irradiation of a conductive solid with multiple identical femtosecond laser pulses, based on the consideration of a hybrid theoretical model. Heat transfer along with hydrodynamics simulations demonstrate that it is possible to create morphology change conditions by solely exploiting capillary effects, in the absence of either non-thermal melting or evaporation. Simulation results, confirmed by experiments, reveal the intermediate surface modification stage acting as a predecessor of microcones formation. .

PACS numbers: 42.25.Hz, 47.20.Dr, 61.80.Az, 64.70.D

Controlling the ultrafast laser-matter interaction processes is crucial for the success and scalability of materials processing applications at micro- and nano- scales opening up several exciting applications in this respect [1, 2]. Materials' processing with ultrashort (subpicosecond) pulsed lasers has received considerable attention over the past decades due to its multiple diverse applications ranging from micro-device fabrication [3] to optoelectronics [4], microfluidics [5-7] and biomedicine [8, 9]. Rapid energy delivery and reduction of the heat-affected areas are the most pronounced advantages of the technique compared to effects induced by longer pulses, which reflect the merit of the method as a promising tool for fabrication at micro- and nano-scales [10]. In view of the abundant applications a thorough knowledge of the laser interaction with the target material is required for enhanced controllability of the structuring process. Crater creation, development of periodic ripples and formation of self-organized micro- or nanocones (spikes) are some of the observable results of surface processing after irradiation of a conductive material with multiple identical subpicosecond lasers pulses. In principle, the first effect is attributed to material removal [11-13] while the second is considered to originate from the superposition of the incident radiation with an electromagnetic wave which is created at a rough relief and scattered along the surface [14]. A conclusive interpretation of the spike formation is still elusive; nevertheless, it is generally accepted that redeposition, ablation effects [15, 16] or evaporation [17, 18] must be incorporated into a scenario that describes the development of such self-organised structures.

Elucidation of the underlying mechanisms that influence the surface modification is achievable through attaining a detailed understanding of the dynamics in irradiated materials from a microscopic point of view. Ultrashort pulsed laser interaction with matter triggers a variety of timescale-dependent processes which are additionally influenced by the pulse duration and fluence [19]. As a consequence, any kind of modification induced is directly dependent on the pulse characteristics, and the type of energy relaxation processes that occur at different timescales which complicates the understanding of the underlying phenomena [20]. Most of studies reported so far, consider that evaporation and non-thermal effects, phenomena which involve processes that occur on subpicosecond time scales, are necessary to produce remarkable surface modification [11, 21, 22]. The primary objective of this Letter is the theoretical and experimental evidence of ultrafast laser induced surface morphology alteration in the absence of the above effects. We show that though we consider laser fluence values that do not suffice to produce material removal or non-thermal melting, they are capable to induce a solid-to-liquid phase transition while subsequent solidification leads to a remarkable modification of the surface profile.

A hybrid, three-dimensional theoretical model is employed to illustrate a possible mechanism that leads to the modification of a silicon surface upon laser irradiation. The theoretical framework comprises (i) a heat transfer component that accounts for the particle dynamics and energy transfer from the carriers to the lattice based on Boltzmann's transport equations [23], and (ii) a hydrodynamics element which aims to explore flow dynamics of molten silicon. Governing

equations that describe the Newtonian fluid flow take into account mass, momentum and energy conservation [24] including Marangoni effects and buoyancy forces [25]. One important aspect that is incorporated into our proposed model is pertinent to the fact that molten material behaves as a metal and thereby a revised two-temperature model has to be applied for material in molten phase [21]. Simulations are firstly performed on an initially flat surface for a p -polarised Gaussian (both spatially and temporally) laser pulse with a single pulse ($NP=1$) of fluence $E_d=0.6\text{J}/\text{cm}^2$ and pulse duration $\tau_p=420\text{fs}$. A detailed description of the theoretical model and simulation parameter values are provided in the Supplementary Material. Calculations yield a maximum value for the carrier density that never reaches a critical value n_c ($\sim 2.7 \times 10^{21}\text{cm}^{-3}$ in Si) required for nonthermal melting (Fig.2a). Furthermore, it appears that the maximum lattice temperature attains a value (1993^0K) which is higher than the temperature required for the material to undergo a solid-to-liquid phase transition, however, it never exceeds the evaporation point ($\sim 3540^0\text{K}$) which would induce the onset of material removal effects.

The solidification process is investigated by analysing the hydrodynamics effect due to the surface tension gradient originated from the spatio-temporal variance of the temperature distribution throughout the molten phase. The surface tension variance leads to the development of flow and capillary waves and it eventually results into depression and rise of the surface in regions of higher and lower temperatures, respectively [24, 26]. The resulting flow of the molten material continues during the liquid-to-solid transition which leads to the formation of a new surface contour and the development of a crater while an elevation of the surface occurs near the edge of the affected area (Fig.2a and Fig.2c). Simulations yield a crater depth value equal to 10.01nm . Due to symmetry, results in one quadrant were sketched.

Irradiation of the non-flat surface with a second pulse will give rise to a surface scattered wave \vec{E}_s which interferes with the incident wave \vec{E}_i (Fig. 1), and produces a spatially modulated energy deposition [14, 27]. Varying energy deposition yields a modulated lattice temperature due to the periodic form (in the space domain) of the electric field components of the two waves. Non uniform temperature distribution along the modified surface produces locally surface tension gradients that are responsible for the rise and depression of molten surface. As a result, periodic structures are developed with an orientation perpendicular to the electric field due to the p -polarisation of the beam. A Finite element method was used in our simulation and results for the ripple size and spacing are illustrated in Fig.2b-d for $NP=2$. Furthermore, ripple height is spatially dependent due to the variation of the gradient of the surface tension that generates the creation of the periodic structures. Bigger variations are expected closer to the centre of the laser beam yielding structures with bigger peaks. In order to measure and investigate quantitatively the changes in the surface profile, theoretical simulations are tested against the experimental data. The measured spatial period is smaller ($\sim 675\text{nm}$) than the wavelength of the beam which can be attributed to an

upward-travelling surface scattered wave [27]. Moreover, theoretical calculations yielded a value ($\sim 692\text{nm}$) very close to the experimental result which demonstrates that the model adequately describes the process.

For pulse numbers higher than $NP=4$, a very significant effect is predicted by simulation results. More specifically, a new form of periodic structures (grooves) are developed which are arranged in a wave-like pattern with an orientation perpendicular to the alignment of the ripples (Fig.3a) Interestingly, they have a spatial periodicity which is higher than the wavelength of the ripples. To explore the underlying mechanism that leads to the formation of these structures, it is important to reflect on the interference of the incident wave with the component of the surface wave on the y - z plane. The distributed energy along the y -axis is spatially modulated with bigger variations that lead to an increased temperature gradient. Thereby, capillary effects will be reinforced compared to the mechanism that induces ripple formation, which will result in an increased periodicity. For $NP<4$, the contribution of the terms associated to the groove development is relatively small and simulation results are close to noise. Results of the groove periodicity from experimental data is shown in Fig.3b based on measurements along a cross section in Fig.3a (vertical *white* line) for $NP=40$. Experimental results yield an average value ($\sim 2.5\mu\text{m}$) which appears to be comparable with the theoretical predictions ($\sim 2.9\mu\text{m}$). Fig.3c illustrates the spatial dependence of the groove height while the morphology of the material surface along the y -axis as a result of the groove formation is depicted in Fig.3d. Experimental data show that intensity (which is correlated to height) varies across the grooves, that is also predicted from our theoretical model; this effect is the consequence of the application of a laser pulse to a previously formed surface profile. Molten material rises to a higher point compared to the result of the previous pulse and solidification on the two sides of the groove leads to the formation of a shallow well on top of the peak. Our theoretical findings suggest that this behaviour is stronger for grooves closer to the spot centre and it starts to disappear at bigger distances. Although similar effects should be present for ripples, the fact that ripple periodicity is smaller make their theoretical prediction and experimental observation difficult to achieve.

Simulation results demonstrate that laser irradiation for $NP\geq 65$ leads to lattice temperatures that exceed the evaporation point while induced carrier densities are higher than n_c . Then, the proposed theoretical model is not directly applicable and corrections associated to nonthermal melting and material removal are required to be incorporated to describe the mechanism that characterises the process.

Fig.4 reveals that further increase in the number of pulses will result in the beginning of groove disintegration while the ripple pattern will not be affected. To our best of our knowledge, a proper justification about this process has not been presented yet, however, its significance is pertinent to the fact that effects on these initially periodic structures will eventually lead to the onset of spike formation. Unlike growing speculation that spikes are generated from the influence of successive

number of pulses on the initial ripples, our model indicates that the formation of periodical structures parallel to the beam polarisation is an intermediate stage. Although formation of spikes is usually attributed to ablation [15], the similarities between our theoretical model and experimental findings could work towards formulating a complete theoretical framework that aims to provide a smooth transition to understand the mechanisms that produce these self-organised structures.

In summary, we have revealed the physical mechanism that accounts for the principal/primary stages of the structuring process taking place upon irradiation of a conductive solid with multiple identical femtosecond laser pulses. The results presented here demonstrate that our proposed hybrid model provides a very good insight into the modification process that dictates the formation of ripples and grooves and yields significant quantitative details of the underlying mechanism. Indeed, the model developed is capable to predict to a good agreement with experiment the characteristics of fs laser induced groove formation, based solely on hydrodynamics principles and in the absence of non-thermal and evaporation effects. Theoretical simulations and experimental observations indicate that depending on the number of pulses to which the material is subjected, the three types of surface modification can be distinguished and temperature dependent surface tension gradients are capable to generate molten material movements that lead to the prominent morphology changes. Our results demonstrate the ability to precisely control and predict the size of the different structures attained by modulating the laser beam characteristics and number of pulses offering a unique opportunity for controllable structuring desired for a wide range of applications in industry and biomedicine. It is envisaged that this work can be proved useful for applications in which the attainable fluences are low, including laser structuring by means of temporally and/or spatially shaped pulses [13] and near-field materials processing.

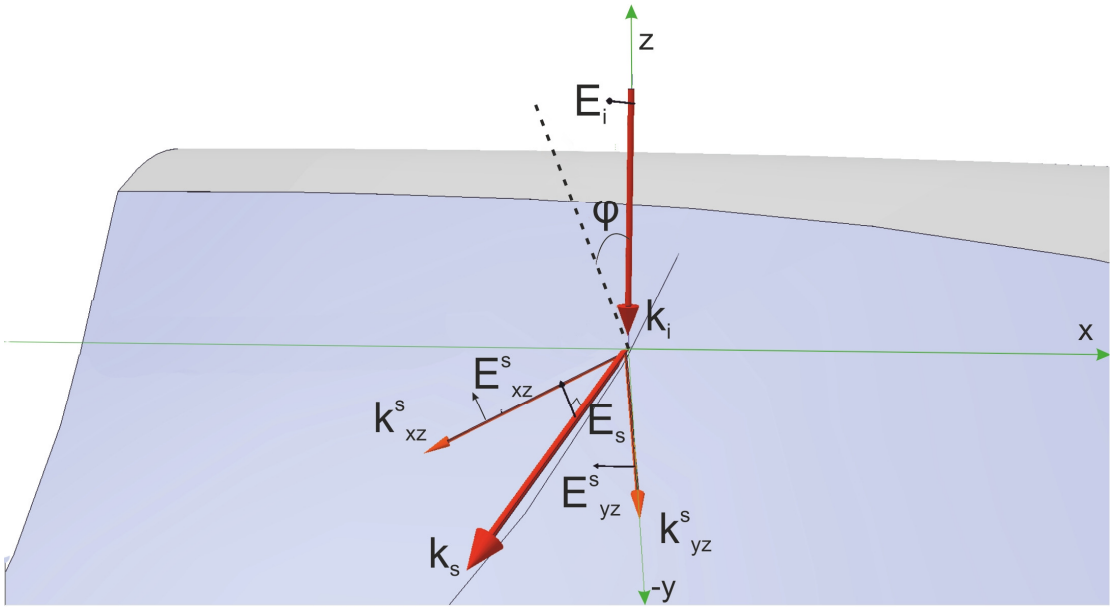
Acknowledgements. The authors acknowledge financial support from the EU.

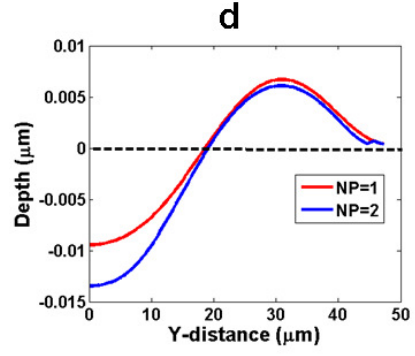
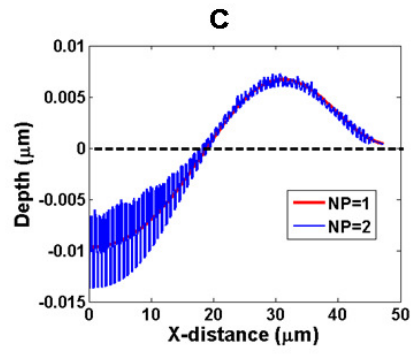
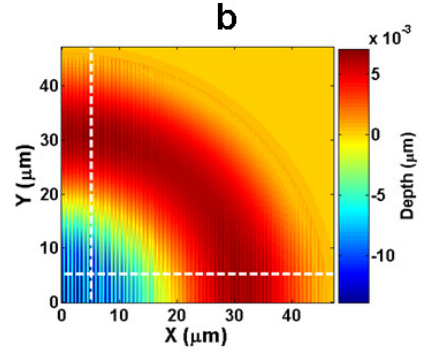
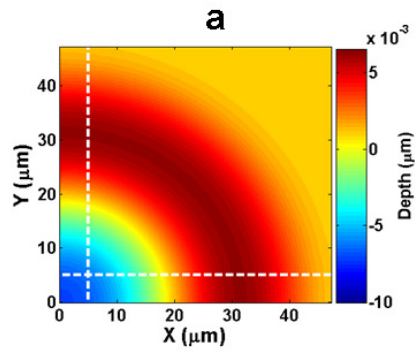
Figure 1: Irradiation of a non-flat Si-surface with a Gaussian beam. Incident (denoted by the index i) and surface scattered waves (denoted by the index s) are depicted. Wave vectors and direction of the electric field (p -polarisation is assumed) of the two waves are sketched. Subscripts xz and yz denote the projection of wave vectors and the electric fields on the xz and yz planes, respectively.

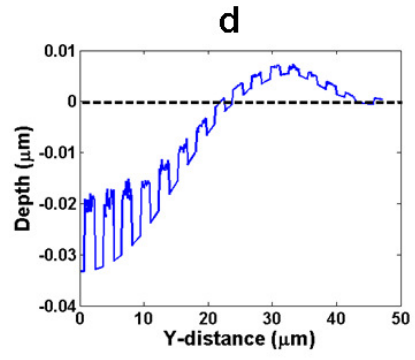
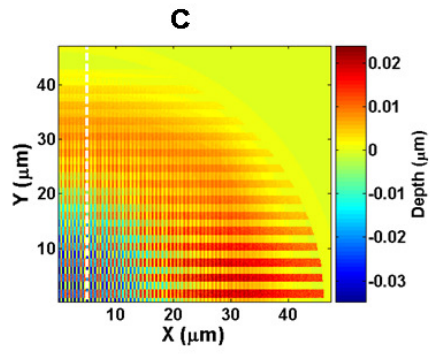
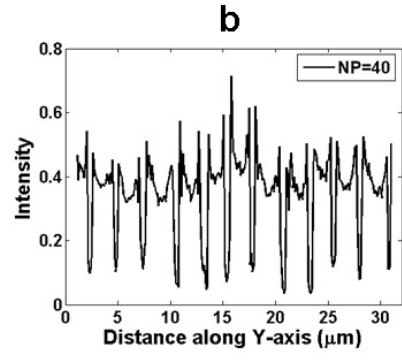
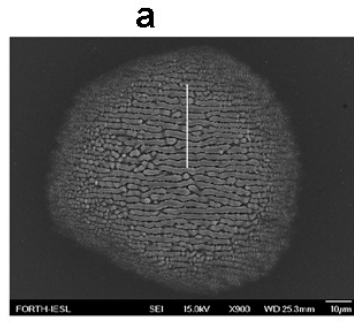
Figure 2: (a) Crater depth contour plot after irradiation with one laser pulse ($NP=1$) for $E_d=0.6\text{J/cm}^2$ and $\tau_p=420\text{fs}$. (b) Ripple formation after irradiation with a second pulse ($NP=2$). (c)-(d) Spatial dependence of ripple height along X-axis (horizontal *white* line) and Y-axis (vertical *white* line) for one (*red* line) and two pulses (*blue* line).

Figure 3: (a) Experimental data for $NP=40$. (b) Groove height along cross section on experimental data. (c) Groove formation for $NP=4$. (d) Spatial dependence of groove height along Y-axis (vertical *white* line).

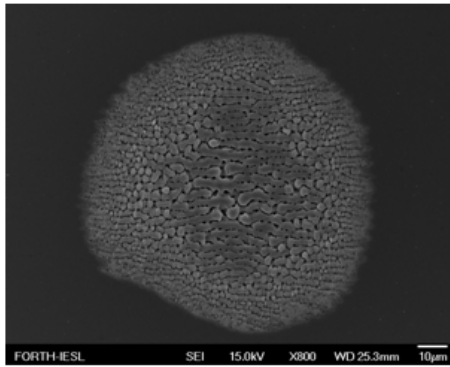
Figure 4: (a) Groove disintegration after 200 pulses. (b) Spike formation after 1600 pulses.



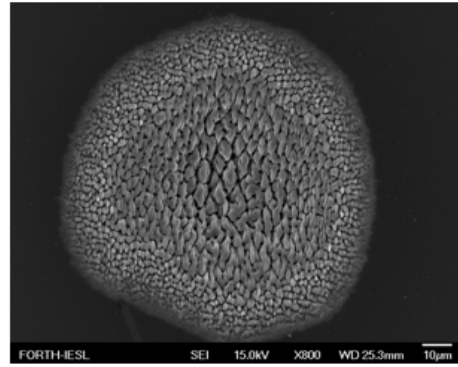




a



b



- [1] D. Bauerle, *Laser Processing and Chemistry* (2nd edition), Springer, Berlin (1996).
- [2] J. C. Diels, and W. Rudolph, *Ultrashort Laser Pulse Phenomena: Fundamentals, Techniques, and Applications on a Femtosecond Time* (2nd edition), Academic Press, Burlington, MA, 2006 (2006).
- [3] V. Zorba *et al.*, *Applied Physics Letters* **88** (2006).
- [4] E. Magoulakis *et al.*, *Applied Physics a-Materials Science & Processing* **98**, 701 (2010).
- [5] V. Zorba *et al.*, *Nanotechnology* **17**, 3234 (2006).
- [6] V. Zorba *et al.*, *Advanced Materials* **20**, 4049 (2008).
- [7] A. Y. Vorobyev, and C. L. Guo, *Optics Express* **18**, 6455 (2010).
- [8] E. Stratakis *et al.*, *Progress in Quantum Electronics* **33**, 127 (2009).
- [9] A. Ranella *et al.*, *Acta Biomaterialia*, doi:10.1016/j.actbio.2010.01.016 (2010).
- [10] R. F. W. Herrmann, J. Gerlach, and E. E. B. Campbell, *Applied Physics a-Materials Science & Processing* **66**, 35 (1998).
- [11] D. Ashkenasi *et al.*, *Applied Physics a-Materials Science & Processing* **77**, 223 (2003).
- [12] J. Bonse, M. Munz, and H. Sturm, *Journal of Applied Physics* **97** (2005).
- [13] R. Stoian *et al.*, *Applied Physics a-Materials Science & Processing* **77**, 265 (2003).
- [14] J. E. Sipe *et al.*, *Physical Review B* **27**, 1141 (1983).
- [15] T. H. Her *et al.*, *Applied Physics Letters* **73**, 1673 (1998).
- [16] A. J. Pedraza, J. D. Fowlkes, and D. H. Lowndes, *Applied Physics Letters* **77**, 3018 (2000).
- [17] S. I. Dolgaev *et al.*, *Applied Surface Science* **253**, 7987 (2007).
- [18] S. I. Dolgaev *et al.*, *Applied Physics a-Materials Science & Processing* **73**, 177 (2001).
- [19] N. M. Bulgakova *et al.*, *Journal of Laser Micro Nanoengineering* **2**, 76 (2007).
- [20] J. T. Zhu *et al.*, *Applied Surface Science* **245**, 102 (2005).
- [21] B. N. Chichkov *et al.*, *Applied Physics a-Materials Science & Processing* **63**, 109 (1996).
- [22] D. P. Korfiatis, K. A. T. Thoma, and J. C. Vardaxoglou, *Journal of Physics D-Applied Physics* **40**, 6803 (2007).
- [23] H. M. van Driel, *Physical Review B* **35**, 8166 (1987).
- [24] L. D. Landau, and E. M. Lifshitz, *Fluid Mechanics* (2nd Edition) (1987).
- [25] L. E. Scriven, and C. V. Sternling, *Nature* **187**, 186 (1960).
- [26] T. R. Anthony, and H. E. Cline, *Journal of Applied Physics* **48**, 3888 (1977).
- [27] G. S. Zhou, P. M. Fauchet, and A. E. Siegman, *Physical Review B* **26**, 5366 (1982).

Supplementary Material

Ultrafast laser induced surface modification in absence of non-thermal melting and evaporation

G. D. Tsiibidis^{1*}, M. Barberoglou¹, P. A. Loukakos¹, E. Stratakis¹, C. Fotakis^{1,2}

¹*Institute of Electronic Structure and Laser (IESL), Foundation for Research and Technology (FORTH), N. Plastira 100, Vassilika Vouton, 70013, Heraklion, Crete, Greece*

²*Physics Department, University of Crete, Heraklion 71409, Crete, Greece*

I. THEORETICAL MODEL

1. Irradiation of a flat surface

Ultrashort-pulses lasers excite the energy carriers (electron-hole) in semiconductors and the energy is transferred to the lattice system. The relaxation time approximation to Boltzmann's transport equation [1] is employed to determine the number density, carrier energy and lattice energy. The model assumes an equal number of electron and holes in the solid and no electron photoemission is considered after the laser irradiation [2]. The evolution of the number density N , carrier temperature T_c and lattice temperature T_l are derived using the carrier balance, carrier energy balance and lattice heat balance. Based on this picture the following set of equations determine the temperature and particle dynamics

$$\begin{aligned}
 C_c \frac{\partial T_c}{\partial t} &= \vec{\nabla} \cdot (k_e + k_h) \vec{\nabla} T_c - \frac{C_c}{\tau_e} (T_c - T_l) + S(\vec{r}, t) \\
 C_l \frac{\partial T_l}{\partial t} &= \vec{\nabla} \cdot (K_l \vec{\nabla} T_l) + \frac{C_c}{\tau_e} (T_c - T_l) \\
 \frac{\partial N}{\partial t} &= \frac{\alpha}{h\nu} \Omega I(\vec{r}, t) + \frac{\beta}{2h\nu} \Omega^2 I^2(\vec{r}, t) - \gamma N^3 + \theta N - \vec{\nabla} \cdot \vec{J} \\
 \Omega &= \frac{1 - R(T_l)}{\cos \varphi}
 \end{aligned} \tag{1}$$

where C_c and C_l are the heat capacity of electron-hole pairs and lattice, respectively, ν is the frequency of the laser beam corresponding to a wavelength equal to $\lambda=800\text{nm}$, k_e and k_h are the thermal conductivity of the electrons and holes, respectively, K_l is the thermal conductivity of the lattice, h is the Plank's constant, γ is the Auger recombination coefficient, θ is the impact ionisation coefficient, α and β are the one-photon and two-photon absorption coefficients, φ is the angle of the incident beam with respect to the normal axis on the irradiated surface, $R(T_l)$ is the reflectivity of the laser beam on the silicon surface (which is a function of the material temperature), τ_e is the energy relaxation time, \vec{J} is the carrier current vector and $S(\vec{r}, t)$ can be interpreted as a generalised 'source' term. The 'source' term is provided by the following expression

$$S(\vec{r}, t) = (\alpha + \theta N) \Omega I(\vec{r}, t) + \beta \Omega^2 I^2(\vec{r}, t) - \frac{\partial N}{\partial t} (E_g + k_b T_c) - N \frac{\partial E_g}{\partial T_l} \frac{\partial T_l}{\partial t} - \vec{\nabla} \cdot ((E_g + 4k_b T_c) \vec{J}) \tag{2}$$

where Θ stands for the free-carrier absorption cross section, k_B is the Boltzmann's constant and E_g the band-gap energy. The contribution of the current vector in the balance equation for the electron-hole carriers depends largely on the pulse duration. Experiments in which damage of Si has been calculated suggest that the divergence of the carrier current for shorter pulses than 600fs can be neglected [3]. The laser intensity in Eqs (1) and (2) is obtained by considering the propagation loss due to one- and two- photon absorption and free carrier absorption [1]

$$\frac{\partial I(\vec{r}, t)}{\partial z} = -(\alpha + \Theta N)I(\vec{r}, t) - \beta I^2(\vec{r}, t) \quad (3)$$

assuming that the laser beam is Gaussian both temporally and spatially and the transmitted laser intensity at the incident surface is expressed in the following form

$$I(r, z = 0, t) = \frac{2\sqrt{\ln 2}}{\sqrt{\pi}\tau_p} E_d e^{-\left(\frac{r^2}{R_0^2}\right)} e^{-4\ln 2 \left(\frac{t-t_0}{\tau_p}\right)^2} \quad (4)$$

where E_d is the fluence of the laser beam and τ_p is the pulse duration (i.e. full width at half maximum), R_0 is the irradiation spot-radius (distance from the centre at which the intensity drops to $1/e^2$ of the maximum intensity); t_0 is chosen to be equal to $3\tau_p$. The choice of the value of t_0 is based on the requirement that at $t=0$, the intensity of the incident beam is practically zero, at $t= t_0$ it reaches the maximum power while laser irradiation vanishes at $t=2t_0$. It is important to emphasise that due to the temperature and spatial dependence of the coefficients in Eq.(3), an independent solution of the form of the intensity beam is not feasible and thereby all Eqs.(1-4) constitutes a set of coupled equations that needs to be solved simultaneously.

Despite the above set of equations yield carrier and lattice temperature spatio-temporal dependence, a modification is required to accommodate the phase transition of the material for fluences that cause the bulk temperature to exceed the silicon melting temperature T_m (~ 1687 °K). While Eqs (1) are valid both for the molten and the solid phase, the second equation has to be altered to include the phase change in the sold-liquid interface

$$(C_l + L\delta_{\pm}(T_l - T_m)) \frac{\partial T_l}{\partial t} = \vec{\nabla} \cdot (K_l \vec{\nabla} T_l) + \frac{C_c}{\tau_e} (T_c - T_l) \quad (5)$$

where L is the latent heat of fusion. The advantage of the introduction of the δ -function is that we can avoid the computation of the temporal change of the liquid fraction [4] f which are included in

the expressions of the enthalpy functions [5]. A suitable representation of the δ -function that accomplishes (for numerical calculations) a smooth transition between solid and liquid phases [6], therefore the following expression is used

$$\delta_{\pm}(T_l - T_m) = \frac{\pm 1}{\sqrt{2\pi}\Delta} e^{-\left[\frac{(T_l - T_m)^2}{2\Delta^2}\right]} \quad (6)$$

where Δ is in the range of 10-100K depending on the temperature gradient. The sign of the δ -function depends on whether melting or solidification takes place. Unlike the solid phase of the irradiated material, liquid silicon behaves as a metal and thereby, for temperatures above T_m , Eqs.1 need to be replaced by the following two equations that describe electron-lattice heat transfer

$$\begin{aligned} C_e \frac{\partial T_e}{\partial t} &= \vec{\nabla} \cdot (K_e \vec{\nabla} T_e) - \frac{C_e}{\tau_E} (T_e - T_L) \\ C_L \frac{\partial T_L}{\partial t} &= \vec{\nabla} \cdot (K_L \vec{\nabla} T_L) + \frac{C_e}{\tau_E} (T_e - T_L) \end{aligned} \quad (7)$$

where C_e and C_L are the heat capacity of electrons and lattice (liquid phase), K_e and K_L are the thermal conductivity of the electrons and lattice, respectively, while τ_E is the energy relaxation time for the liquid phase. Since $K_L \ll K_e$ in metals, the first term of the second part of the second equation is usually ignored. In Eqs. 7, no source term is included because it is assumed that laser energy deposition has been completed before the onset of the material melting.

After heat transfer from electrons to the lattice, a spatio-temporal variance of temperature distribution takes place on the molten material and variation of the surface tension and gravitational force result in the development of flow and capillary waves [7]. The governing equations for the incompressible Newtonian fluid flow and heat transfer in the molten material are defined by the following equations:

(i). for the mass conservation (applied to an incompressible fluid):

$$\vec{\nabla} \cdot \vec{u} = 0 \quad (8)$$

(ii). for the momentum conservation:

$$\rho_L \left(\frac{\partial \bar{u}}{\partial t} + \bar{u} \cdot \bar{\nabla} \bar{u} \right) = \bar{\nabla} \cdot (-P \mathbf{1} + \mu \bar{\nabla} \bar{u}) + \rho_{L0} (1 - \beta_t (T_L - T_m)) \bar{g} \quad (9)$$

(iii). for the energy conservation

$$C_L \left(\frac{\partial T_L}{\partial t} + \bar{\nabla} \cdot (\bar{u} T_L) \right) = \bar{\nabla} \cdot (K_L \bar{\nabla} T_L) \quad (10)$$

where \bar{u} is the velocity of the fluid, P is the pressure, ρ_L and ρ_{L0} are the densities of the molten material at temperatures T_L and T_m , respectively, β_t is the coefficient of thermal expansion. C_L and K_L stand for the heat capacity and thermal conductivity of the liquid phase, respectively. The equilibrium between the carrier and lattice temperatures indicates that there is no more heat transfer between the two subsystems and thereby Eq.10 replaces the second of Eq.1. Eq.10 takes the following form at the solid-liquid interface to denote the resolidification process

$$C_L \left[\frac{\partial T_L}{\partial t} + \bar{\nabla} \cdot (\bar{u} T_L) \right] + L \delta_- (T_L - T_m) \frac{\partial T_L}{\partial t} = \bar{\nabla} \cdot (K_L \bar{\nabla} T_L) \quad (11)$$

For a Gaussian beam with a radial dependence, temperature decreases as the distance from the centre of the beam increases; at the same time, the surface tension in pure molten silicon decreases with growing melt temperature (i.e $d\sigma/dT < 0$), which causes the depression of the surface of the liquid closer to the maximum value of the beam while it rises elsewhere. In other words, spatial surface tension variation induces stresses on the free surface and therefore a capillary fluid convection is produced. The generated ripple height is calculated from the Saint-Venant's shallow water equation [8]

$$\frac{\partial H(\vec{r}, t)}{\partial t} + \bar{\nabla} \cdot (H(\vec{r}, t) \bar{u}) = 0 \quad (12)$$

where $H(\vec{r}, t)$ stands for the melt thickness. The above equations will yield the profile of the surface of the material upon solidification.

2. Interference of an incident with a surface-scattered wave

Due to an inhomogeneous deposition of the laser energy on the semiconductor as a result of the exposure to a Gaussian-shape beam, the surface of material is not expected to be flat; further

irradiation of the non-flat profile will give rise to a surface scattered wave[9]. According to theoretical predictions and experimental studies, the interference of the incident and the surface wave results in the development of ‘ripples’ with orientation either perpendicular (p -polarisation) or parallel (s -polarisation) to the electric field of the laser beam [9-11]. The wavelength of the ripples is $\lambda(1 \pm \sin\phi)$, for p -polarisation and $\lambda \cos\phi$, for s -polarisation [10, 11]. The minus sign in the first expression is produced by the interference of the incident wave with a downward-travelling surface wave [11]. By contrast, the plus sign is related to the interference with an upward-travelling surface wave that yields a ripple wavelength which is bigger than the laser wavelength. Furthermore, the ripple wavelength produced by a beam which is s -polarised is always bigger than the beam wavelength.

For simplicity reasons, in the present work, we consider a p -polarised incident beam. Although the equations presented in the previous section are still valid, some modification has to be performed to accommodate the interference of the incident and the scattered wave [12]. The total average intensity of the two waves on the surface of the material (i.e. at $z=0$) is derived by computing the total Poynting vector and integrating it over the laser period (λ/c). Then, the total Poynting vector on the surface can be computed from the following expression

$$\langle S \rangle \sim \left((\vec{E}_i)^2 + (\vec{E}_s)^2 + 2\vec{E}_i \cdot \vec{E}_s \cos\left(\frac{2\pi}{\lambda}(t - 3\tau_p) + (\vec{k}_i + \vec{k}_s) \cdot \vec{r}\right) \right) \quad (13)$$

II. SIMULATION

The proposed model aims to determine the time-dependent surface shape by solving both momentum and energy equations introduced in the previous paragraphs. It takes into account Marangoni effect [13] and buoyancy forces, latent heat of fusion and phase transition, however, it neglects evaporation due to the fact that the number of pulses used ($NP \leq 65$) and the fluence of each single pulse $E_d = 0.6 \text{ J/cm}^2$ are not sufficient for the surface temperature to exceed the evaporation point ($T_{\text{evap}} = 3540 \text{ K}$). As a result, hydrodynamics effects are assumed to be the only factor that leads to the change of the material morphology. Because of the anticipated surface modification, a finite difference method to solve the Eqs.(1-13) will produce inaccurate results and therefore a finite element method is employed.

Simulation of the crater formation after irradiation of a flat surface with a single pulse ($NP=1$) is easier to perform due to the symmetry of the problem. Symmetry suggests that Eqs. (1-13) can be solved along the r and z axes to obtain the carrier and lattice temperatures and the surface

modification details. Due to the cylindrical symmetry, we assume that quantities in the above set of equations dependent on the depth and the radial distance. As a result, in our calculation, we can consider that the first pulse irradiates a rectangular region of thickness $W=2\mu\text{m}$ and length $L=140\mu\text{m}$ and the simulations run from $t=0$ to 200ns. Carriers and lattice temperatures are set to $T=T_0=300^0\text{K}$ (room temperature) at $t=0$. The population of conduction electrons for a semiconductor at $T=T_0$ is given by the expression

$$N_e(t=0) = \frac{2^{5/2} (m_e k_B T_0)^{3/2}}{h^3} T_0^{3/2} e^{-E_g^0/(2k_B T_0)} \quad (15)$$

where m_e is the electron mass, E_g^0 is the energy gap between the conduction and the valence bands in the semiconductor at $T=T_0$. In an intrinsic silicon semiconductor, $N=N_e=N_{holes}=0.98 \times 10^{16} \text{ m}^{-3}$ at $t=0$. The need to investigate surface modification requires the investigation of the movement of the molten material and the interface between the liquid and solid phase. As mentioned above, the solid to liquid transition is accompanied by the change in the material characteristics. During the ultrashort period of laser heating, heat loss from the upper surface of target is assumed to be negligible. As a result, the heat flux boundary conditions for carriers and lattice are zero throughout the simulation while a zero flux at $r=0$ must be also imposed. Furthermore, it is assumed that only the top surface is subjected to the Gaussian-shape laser beam of an irradiation spot-radius $R_0=39.52\mu\text{m}$. Regarding the momentum conditions at the boundaries, we impose the following constraints:

1. $u_r=0$, on the symmetry axis $r=0$,
2. $u_z=0$, on the top side (when the top surface has not melted),
3. $\vec{u} = 0$, on the solid-liquid interface (non-slipping conditions),
4. $\mu \frac{\partial u_r}{\partial z} = \frac{\partial \sigma}{\partial T_s} \frac{\partial T_s}{\partial r}$, on the top surface (T_s is the surface temperature),
5. $P=0$, on the top surface.

In Fig.3a, we notice that the carrier temperature initially rises rapidly before it reaches a peak, it subsequently decreases slightly and then, it soars to much higher maximum value. Similar behaviour has been reported in previous works and it was attributed to ongoing Auger recombination process [14, 15]. The equilibrium between the lattice and the carrier temperatures occurs near $t=5\text{ps}$. The simulation for the above values of the fluence and pulse duration yields a maximum value for the carrier density that never reaches a critical value n_c ($\sim 2.7 \times 10^{21} \text{ cm}^{-3}$ in Si) which is important for nonthermal melting consideration (Fig.3b). Furthermore, it appears (Fig.3a) that the maximum lattice temperature attains a value (1993K) which is bigger than the temperature

required for the material to undergo a solid-to-liquid phase transition, however, it never exceeds the evaporation point which would induce the onset of ablation effects. As a result, one single pulse is not capable to produce either ablation or nonthermal melting. The spatial dependence of the lattice temperature at $t=3\text{ps}$ is depicted in Fig.3c and Fig.3d presents contour maps which illustrate the shape of the isothermal lines. It appears that the contour lines of the lattice temperatures have a smooth oval form. Although the simulation has been performed in a bigger region ($140\mu\text{m} \times 2\mu\text{m}$) we present images of smaller areas to allow a more detailed investigation of melting and resolidification. Fig.4 illustrates the dependence of the carrier temperature and densities on the laser characteristics. Due to bigger energy deposition at higher fluences, a rise in the carrier temperature and densities is expected (Fig.4a,b). Similarly, if the pulse duration increases to 1ps for the same fluence, the energy deposition occurs within a bigger period which leads to smaller values for the temperature and density (Fig.4c,d). The introduction of t_0 in Eq.4 entails on plotting quantities with respect to the dimensionless variable t/τ_p , otherwise their initial rise are shifted to later times which would lead to misleading results. Regarding the behaviour at different values of the pulse duration, we notice that the maximum temperature and densities occur slightly at smaller values of the variable t/τ_p .

The temperature-dependent parameters that are used in the numerical solution of the governing equations are listed in Table I. In order to reduce the computation time, momentum equations that correspond to the molten phase are solved in the region close to the heat source. Therefore, the model geometry is properly divided into two regions: a subdomain in which only the momentum equations are solved and another subdomain where both momentum and energy equations are solved. To compute the size of the resolidified material, melting kinetics (molten material thickness and liquid/solid interface velocity) are also computed. The top boundary was discretised with a maximum element size 20nm while the maximum element size for the fluid subdomain was set to 5nm. A time-dependent solver was used together with a direct linear system solver.

It is important to emphasise that the above boundary conditions are valid in the first simulation where the initial profile of the top surface is flat. The first two boundary conditions exclude transverse and lateral components of the velocity on the symmetry axis ($r=0$) and the top surface, while the left part of the fourth constraint represent the shear stress on the surface of the material. Although a similar procedure is ensued in the event of a modified surface profile which is expected as a result of the movement of the molten material and its subsequent resolidification, proper attention is necessary which is associated to morphology change. Due to fact that the incident beam, in principle, is not normal to the modified profile, we have to take into account that in some parts of the material there exist an accumulation of energy that reaches the surface which originates from

both the incident fluence and the reflection from another part of the surface. Moreover, the absorbed energy is directly dependent on the angle at which the incident beam irradiates the material. Typical Fresnel equations are used to describe the reflection and transmission of the incident light. With respect to the boundary conditions, tangential component of the velocity on the top side is zero while the fourth boundary condition has to be replaced by the equation $\mu \frac{\partial u_s}{\partial Z_{new}} = \frac{\partial \sigma}{\partial T_s} \frac{\partial T_s}{\partial R_{new}}$, where u_s is the tangent component of the velocity on the surface of the material while R_{new} and Z_{new} represent the tangential and vertical axes on a moving reference frame.

III. EXPERIMENTAL DETAILS

Laser-fabricated spots on flat Si surfaces were performed by femtosecond (fs) laser irradiation in vacuum, and different surface topologies were obtained by varying the number of pulses at two laser fluences. Single crystal n-type Si(100) wafers with a resistivity of 2-8 Ohm-cm were placed inside a vacuum chamber that was evacuated down to a base pressure of 10-2 mbar at the beginning of each run. The irradiating source was a regenerative amplified Ti:Sapphire laser ($\lambda=800$ nm) delivering pulses at a repetition rate of 1 kHz and pulse duration at 420fs, measured with the Frequency Resolved Optical Gating (F.R.O.G.) technique. Samples were mounted on a high-precision X-Y translation stage normal to the incident laser beam. A mechanical shutter was synchronized to the stage motion and provided spots with desired number of laser pulses, controlled by a computer. The laser pulse fluence used was $0.4\text{J}/\text{cm}^2$ and $0.6\text{J}/\text{cm}^2$. For the calculation of the laser fluence, the laser beam was focused with a 30cm lens and monitored on a CMOS camera. The intensity distribution obtained was afterwards analyzed by an image processing algorithm and the spot diameter calculated at the beam waste yielded a value of $80\mu\text{m}$.

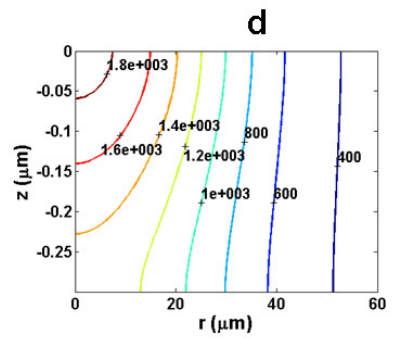
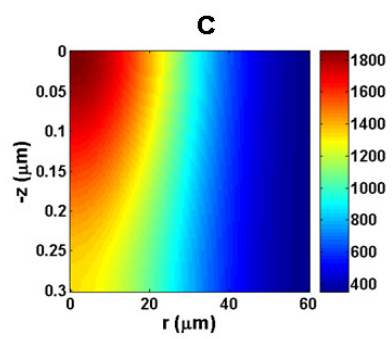
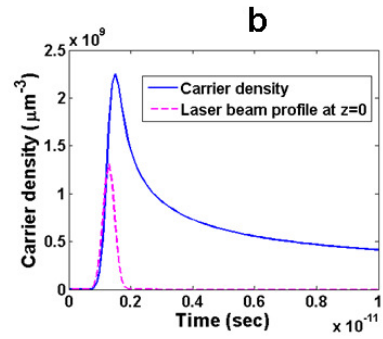
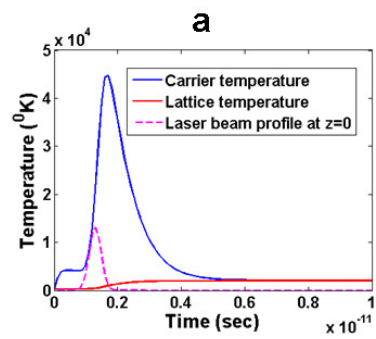
- [1] H. M. van Driel, *Physical Review B* **35**, 8166 (1987).
- [2] T. Held, T. Kuhn, and G. Mahler, *Physical Review B* **44**, 12873 (1991).
- [3] P. P. Pronko *et al.*, *Physical Review B* **58**, 2387 (1998).
- [4] N. M. Bulgakova *et al.*, *Applied Physics a-Materials Science & Processing* **81**, 345 (2005).
- [5] Y. Zhang, and J. K. Chen, *Applied Physics a-Materials Science & Processing* **88**, 289 (2007).
- [6] C. P. Grigoropoulos, R. H. Buckholz, and G. A. Domoto, *Journal of Applied Physics* **60**, 2304 (1986).
- [7] T. R. Anthony, and H. E. Cline, *Journal of Applied Physics* **48**, 3888 (1977).
- [8] L. D. Landau, and E. M. Lifshitz, *Fluid Mechanics* (2nd Edition) (1987).
- [9] J. E. Sipe *et al.*, *Physical Review B* **27**, 1141 (1983).
- [10] B. Tan, and K. Venkatakrishnan, *Journal of Micromechanics and Microengineering* **16**, 1080 (2006).
- [11] G. S. Zhou, P. M. Fauchet, and A. E. Siegman, *Physical Review B* **26**, 5366 (1982).
- [12] D. J. Jackson, *Classical Electrodynamics* (3rd Edition) (1998).
- [13] L. E. Scriven, and C. V. Sternling, *Nature* **187**, 186 (1960).
- [14] J. K. Chen, D. Y. Tzou, and J. E. Beraun, *International Journal of Heat and Mass Transfer* **48**, 501 (2005).
- [15] S. H. Lee *et al.*, *Numerical Heat Transfer Part a-Applications* **44**, 833 (2003).
- [16] D. Agassi, *Journal of Applied Physics* **55**, 4376 (1984).
- [17] R. F. Wood, and G. E. Giles, *Physical Review B* **23**, 2923 (1981).
- [18] J. R. Meyer, M. R. Kruer, and F. J. Bartoli, *Journal of Applied Physics* **51**, 5513 (1980).
- [19] D. P. Korfiatis, K. A. T. Thoma, and J. C. Vardaxoglou, *Journal of Physics D-Applied Physics* **40**, 6803 (2007).
- [20] M. Neuberger, *Handbook of Electronic Materials*, (IFI/Plenum, New York) **Vol. 5**, p. 36 (1971).
- [21] D. P. Korfiatis, K. A. T. Thoma, and J. C. Vardaxoglou, *Applied Surface Science* **255**, 7605 (2009).
- [22] Y. Okano *et al.*, *International Journal of Applied Electromagnetics and Mechanics* **18**, 187 (2003).
- [23] Y. Sato *et al.*, *International Journal of Thermophysics* **21**, 1463 (2000).

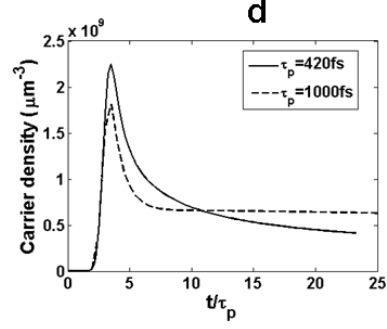
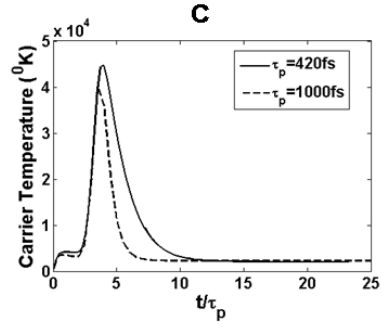
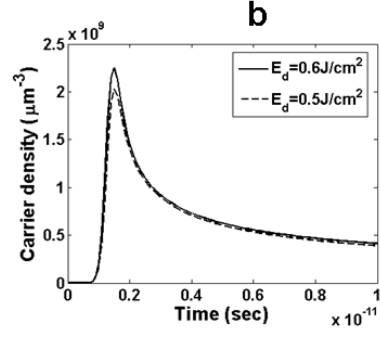
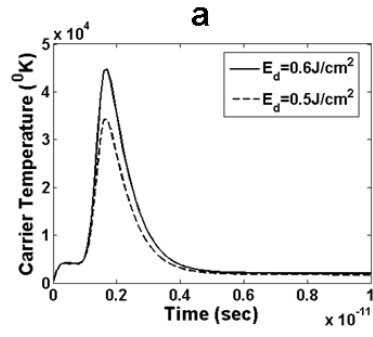
TABLE I. Model parameters for Si.

Solid Phase		
Quantity	Symbol (Units)	Value
Initial temperature	T_0 (°K)	300
Electron-hole pair heat capacity	C_e (J/ μm^3 K)	$3Nk_B$
Electron-hole pair conductivity [16]	K_e (W/ μm K)	$10^{-6} \times (-0.5552 + 7.1 \times 10^{-3} \times T_e)$
Lattice heat capacity [17]	C_l (J/ μm^3 K)	$10^{-12} \times (1.978 + 3.54 \times 10^{-4} \times T_l - 3.68 T_l^{-2})$
Lattice heat conductivity [17]	K_l (W/ μm K)	$0.1585 T_l^{-1.23}$
Band gap energy [18]	E_g (J)	$1.6 \times 10^{-19} \times (1.167 - 0.0258 T_l / T_0 - 0.0198 (T_l / T_0)^2)$
Interband absorption (800nm) [19]	α (μm^{-1})	$0.112 e^{T_l/430}$
Two-photon absorption (800nm) [19]	β (sec/J)	9×10^{-5}
Reflectivity (800 nm) [19]	$R(T_l)$	$0.329 + 5 \times 10^{-5} T_l$
Latent heat of melting [20]	L_m (J/ μm^3)	4206×10^{-12}
Melting temperature [20]	T_m (K)	1687
Auger recombination coefficient [1]	γ ($\mu\text{m}^6/\text{sec}$)	3.8×10^{-7}
Impact ionisation coefficient [1]	θ (sec $^{-1}$)	$3.6 \times 10^{10} e^{-1.5E_e/k_B T_e}$
Free carrier absorption cross section (800nm) [19]	Θ (μm^2)	$2.56 \times 10^{-10} T_l / T_0$
Energy relaxation time [16]	τ_e (sec)	$\tau_{e0} \left[1 + \left(\frac{N}{N_{cr}} \right)^2 \right]$, $\tau_{e0} = 0.5 \times 10^{-12}$ sec, $N_{cr} = 2 \times 10^9 \mu\text{m}^{-3}$
Molten Phase		
Electron heat capacity [21]	C_e (J/ μm^3 K)	$10^{-16} \times T_e$
Electron conductivity [21]	K_e (W/ μm K)	67×10^{-6}
Lattice heat capacity [22]	C_L (J/gr K)	$1.06 \rho_L$
Density [23]	ρ_L (gr/ μm^3)	$10^{-12} \times (3.005 - 2.629 \times 10^{-4} T_L)$
Dynamic viscosity [22]	μ (mPa sec)	0.9
Thermal Expansion coefficient [22]	β_l (K $^{-1}$)	1.32×10^{-4}
Temperature coefficient of surface tension [22]	$d\sigma/dT$ (N/m K)	-0.13
Energy relaxation time [1]	τ_E (sec)	10^{-12}

Figure 1: Results for one laser pulse ($NP=1$) for $E_d=0.6\text{J}/\text{cm}^2$ and $\tau_p=420\text{fs}$. (a) Time evolution of the maximum values of the carrier and lattice temperatures (dashed line represents form of the laser beam profile at $z=0$), (b) Evolution of the maximum values of the carrier density, (c) Spatial distribution of lattice temperatures at $t=3\text{ps}$, (d) Contours plot of the lattice temperatures at $t=3\text{ps}$.

Figure 2: Results for one laser pulse ($NP=1$). Time evolution of the maximum values of the carrier temperatures (a) and densities (b) at $z=0$ for $E_d=0.5\text{J}/\text{cm}^2$ and $E_d=0.6\text{J}/\text{cm}^2$ at $\tau_p=420\text{fs}$. Time evolution of the maximum values of the carrier temperatures (c) and densities (d) at $z=0$ at $E_d=0.6\text{J}/\text{cm}^2$ for $\tau_p=420\text{fs}$ and $\tau_p=1\text{ps}$.





* Corresponding author, E-mail address: tsibidis@iesl.forth.gr

* Corresponding author, E-mail address: tsibidis@iesl.forth.gr